Energy & Environmental Science

# Hydrogen Generation via Ammonia Decomposition on Highly Efficient and Stable Ru-free Catalysts: Approaching Complete Conversion at 450 oC

| | |
|---|---|
| Journal: | *Energy & Environmental Science* |
| Manuscript ID | EE-ART-12-2021-003730.R2 |
| Article Type: | Paper |
| Date Submitted by the Author: | 07-Jul-2022 |
| Complete List of Authors: | Tabassum, Hassina; University at Buffalo, Chemical and Biological Engineering<br>Mukherjee, Shreya ; University at Buffalo, Chemical and Biological Engineering<br>Chen, Junjie; University at Buffalo - The State University of New York, Chemical and Biological Engineering<br>Holiharimanana, Domoina; Southern Illinois University System<br>Karakalos, Stavros; University of South Carolina, College of Engineering and Computing<br>Yang, Xiaoxuan; University at Buffalo, Chemical and Biological Engineering<br>Hwang, Sooyeon; Brookhaven National Laboratory, Center for Functional Nanomaterials<br>Zhang, Tianyu; Southern Illinois University System<br>Lu, Bo; Bettergy corp<br>Chen, Min; Bettergy corp<br>Zhong, Tang; Bettergy corp<br>Kyriakidou, Eleni; University at Buffalo - The State University of New York, Chemical and Biological Engineering Department<br>Ge, Qingfeng; Southern Illinois University, Department of Chemistry and Biochemistry<br>Wu, Gang; University at Buffalo, Chemical and Biological Engineering |
| | |

# Hydrogen Generation via Ammonia Decomposition on Highly Efficient and Stable Ru-free Catalysts: Approaching Complete Conversion at 450 ºC

Hassina Tabassum,[+,1] Shreya Mukherjee,[+,1] Junjie Chen,[+,1] Domoina Holiharimanana,[+,2] Stavros Karakalos,[3] Xiaoxuan Yang,[1] Sooyeon Hwang,[4,*] Tianyu Zhang,[2] Bo Lu,[5] Min Chen,[5] Zhong Tang,[5] Eleni A. Kyriakidou,[1,*] Qingfeng Ge,[2,*] and Gang Wu[1,*]

[1]Department of Chemical and Biological Engineering, University at Buffalo, The State University of New York, Buffalo, New York 14530, USA. Email: gangwu@buffalo.edu (G.Wu) and elenikyr@buffalo.edu (E.A. Kyriakidou)

[2]Department of Chemistry and Biochemistry, Southern Illinois University, Carbondale, Illinois 62901, USA. Email: qge@chem.siu.edu (Q. Ge)

[3]Department of Chemical Engineering, University of South Carolina, Columbia, South Carolina 29208, USA

[4]Center for Functional Nanomaterials, Brookhaven National Laboratory, Upton, New York 11973, USA. Email: soohwang@bnl.gov (S. Hwang)

[5]Bettergy Corp., Peekskill, New York 10566, USA

[+]These authors contributed equally

*Corresponding authors

**Broader Context**

The development of clean and carbon-neutral hydrogen energy technologies is crucial for the energy and environmental sustainability of human civilization. However, hydrogen still faces grand challenges in production, transportation, distribution, and storage. As a hydrogen carrier, ammonia has been recognized as a vital carbon-neutral liquid fuel and distributed energy storage because it is a widely used chemical for many purposes and can be handled safely. Among advanced ammonia energy technologies, ammonia decomposition (*i.e.*, cracking) at economical temperatures (*i.e.*, < 450 $^{o}$C) is critical to on-site hydrogen generation to bypass challenging hydrogen transportation and storage. Currently, ammonia decomposition relays on expensive Ru-based catalysts at higher temperatures, which are not feasible and economical for scale-up and wide applications. Herein, we reported a highly active and stable Ru-free catalyst from earth-abundant elements for efficient carbon-free hydrogen generation via ammonia decomposition. A complete ammonia conversion to hydrogen was achieved at an economically feasible 450 $^{o}$C over the inexpensive catalyst. Outstanding catalytic stability was demonstrated in an industry membrane reactor up to 600 hours, holding a great promise for efficient on-site clean hydrogen generation via the feasible ammonia decomposition.

**Abstract**

Hydrogen ($H_2$) is a prospective zero-carbon, high-energy-density fuel to generate power and clean energy instead of using fossil fuels. Ammonia ($NH_3$) is a promising $H_2$ (17.7%) carrier which can easily overcome the disadvantages related to its storage and transportation. Thermocatalytic ammonia decomposition reaction (ADR) is an effective way to obtain clean $H_2$ but relied on the usage of expensive and rare ruthenium (Ru)-based catalysts, which is not sustainable and economically feasible. Herein, we report a novel synergistic strategy to design a heterostructured Ru-free catalyst, consisting of CoNi alloy nanoparticles well-dispersed on MgO-$CeO_2$-SrO mixed oxide support with further potassium promotion. The K-$CoNi_{alloy}$-MgO-$CeO_2$-SrO catalyst presents 97.7% and 87.50% $NH_3$ conversion efficiency at 450 $^oC$ in GHSV of 6000 mL $h^{-1}$ $g_{cat}^{-1}$ and 12000 mL $h^{-1}$ $g_{cat}^{-1}$, respectively. At 500 $^oC$, the $H_2$ production rate (57.75 mmol $g_{cat}^{-1}$ $min^{-1}$) becomes comparable to most of the reported Ru-based catalysts. The catalyst stability has been successfully demonstrated in both a fixed-bed reactor under high pressure (120 h at 5.0 bar) and a membrane reactor prototype (600 h at 1.5 bar) at 500 $^oC$. High-temperature in-situ XPS analysis, temperature-programmed desorption/reduction, and density functional theory calculations have been carried out to elucidate the possible active sites and performance enhancement mechanisms. This work highlights the importance of constructing optimal interfaces between active metal nanoparticles and oxide support for boosting the $NH_3$ to $H_2$ conversion efficiency and long-term stability.

**Keywords:** Ammonia decomposition reaction; ammonia cracking; hydrogen generation; heterogeneous catalysis; mixed oxide support.

## 1. Introduction

Nowadays, renewable energy and sustainability have become a top concern of the C-suite agenda around the world, as such, they have committed to making an unequivocal response to curb the rising climate change.[1-3] Hydrogen ($H_2$) has received considerable attention and leading positions as a clean energy source in zero-emission vehicles, auxiliary power units, and industrial applications because of its highest gravimetric energy density.[4-6] However, energy-intensive $H_2$ storage and transportation currently are significant hurdles in developing hydrogen-based technologies such as fuel cells.[7-9] Thus, efficient, low-cost, and sustainable technologies for $H_2$ production, storage, and transportation are highly desirable and urgent.[10-12] Thermal ammonia ($NH_3$) decomposition reaction (ADR) (*i.e.*, ammonia cracking) for hydrogen generation has taken a promising place in clean energy resources because of the high hydrogen content (17.8%) and facile liquefication of $NH_3$ at low pressure (8.6 bar) and temperature (20 $^oC$).[13-15] Highly efficient and durable catalysts are crucial for the ADR at low temperatures with complete conversion of inlet-$NH_3$ gas.[16] Traditionally, ruthenium (Ru) is a well-known metal catalyst for catalyzing the ADR, but its commercial-scale applications are impeded because of its scarcity and high cost.[17] Significant efforts have been made to reduce the cost of catalysts by dispersing Ru nanoparticles on various support, including carbon nanotubes and metal oxides. However, these catalysts still can not meet the demands of the industry due to the incomplete conversion efficiency at economically feasible temperatures (<450 $^oC$), insufficient stability, and remaining cost issues.[16, 18, 19] Replacing the expensive Ru catalysts with earth-abundant elements would accelerate the global scalability of such promising ammonia cracking technology for clean on-site hydrogen generation.[20] Thus, the exploration of inexpensive, plentiful, highly active, and durable catalysts from earth-enriched metals for the ADR has been crafted with great significance in the past decade.[13, 20-25]

Recently, heterostructured catalysts with active metals (*e.g.*, Co, Ni, or Fe), high surface area support (*e.g.*, CaNH, $Al_2O_3$, and $SiO_2$), and electron-donating promoters (*e.g.*, Ce, La, Na, and K) have been broadly studied for improving ADR activity.[21, 26, 27] Among the myriad of existing catalysts, the bimetallic (*e.g.*, NiFe and CoMo) alloys with selected support and promoters have been identified as promising candidates for the ADR as compared to the monometallic active phases.[21, 28, 29] Generally, the support can stabilize metallic nanoparticles to increase active site density and regulate surface chemistry to facilitate intermediates diffusion during the reaction.[21] Particularly, the optimal basicity of the heterostructure catalyst enhances the catalytic activity and ability to form diatomic nitrogen bonding during ADR. In addition, alkali metals have been identified as promoters that enhance the activity compared to unpromoted catalysts.[16] However, selecting appropriate active metals, support, promoter, and their interfaces with optimal stoichiometry remain a grand challenge to achieve adequate activity and stability for the ADR. [21]

Herein, we report a synergistic strategy for constructing a heterostructured catalyst based on active metals, oxide support, and promoter as high-performance Ru-free catalysts. The catalyst consists of CoNi alloy nanoparticles dispersed on mixed oxide support of magnesium (Mg), cesium (Ce), and strontium (Sr) modified with K promoters, denoted as K-$CoNi_{alloy}$-MgO-$CeO_2$-SrO, which yields a synergy to promote the ADR significantly. At an economically feasible temperature, *i.e.*, 450 $^oC$, the best performing catalyst presents 97.7% and 87.5% $NH_3$ conversion efficiency at gas hourly space velocity (GHSV) values of 6000 and 12000 mL $h^{-1}$ $g_{cat}^{-1}$, respectively. An encouraging $H_2$ production rate of 57.75 mmol $g_{cat}^{-1}$ $min^{-1}$ was achieved at 500 $^oC$ with complete conversion, comparable to most of the studied Ru-based catalysts. More

importantly, the Ru-free catalyst has been successfully transferred in a prototype membrane reactor, showing exceptional stability up to 600 h under 1.5 bar at 500 $^{o}$C.

## 2. Results and discussion

### 2.1 Catalyst synthesis, morphology, and structures

The heterostructured K-promoted $CoNi_{alloy}$-MgO-$CeO_2$-SrO catalyst was synthesized by developing a facile and scalable synthetic method via co-precipitation and thermal activation. Briefly, metal nitrate hydrates of Mg, Sr, and Ce were dissolved in an aqueous solution with an optimal molar ratio of 2:1:1. Meanwhile, Co and Ni nitrate salts were added to the solution with a total loading of 60 wt.% against support oxides. Then, the solution was added to a KOH solution (*i.e.*, 4 M) dropwise, followed by an aging process without stirring. The formed precipitates were then separated by centrifuging followed by washing with water. The resulting powder was dried, pulverized, and treated under forming gas at 600 $^{o}$C for one hour to obtain the final catalyst. As a result, Co and Ni were fully reduced to form CoNi alloy nanoparticles dispersed on the mixed oxide support containing Mg, Sr, and Ce with K modification. Meanwhile, it is also possible that minor Ni and Co species could be incorporated into the mixed oxide support. The detailed synthesis procedures were provided in the Electronic supplementary information (ESI). As a comparison, control catalyst samples were synthesized with different stoichiometry and elemental compositions of support and active materials, including $CoNi_{alloy}$-MgO-$CeO_2$, $CoNi_{alloy}$-MgO, $CoNi_{alloy}$-SrO, $CoNi_{alloy}$ (without support), and mono-metals (Co, Ni) with support (Co-MgO-$CeO_2$-SrO and Ni-MgO-$CeO_2$-SrO). Different ratios for active materials Co on the optimal support of MgO-$CeO_2$-SrO were also studied concerning catalytic activity under different conditions. Various concentrations of KOH used for the K-$CoNi_{alloy}$-MgO-$CeO_2$-SrO catalyst synthesis were also investigated in terms of the basicity of the catalysts

and measured corresponding catalytic activity because K could act as an electron-donating element and promote the ADR activity. In addition, K was replaced with Cs as a possible promoter, and the corresponding sample Cs-$CoNi_{alloy}$-MgO-$CeO_2$-SrO was also studied for the ADR.

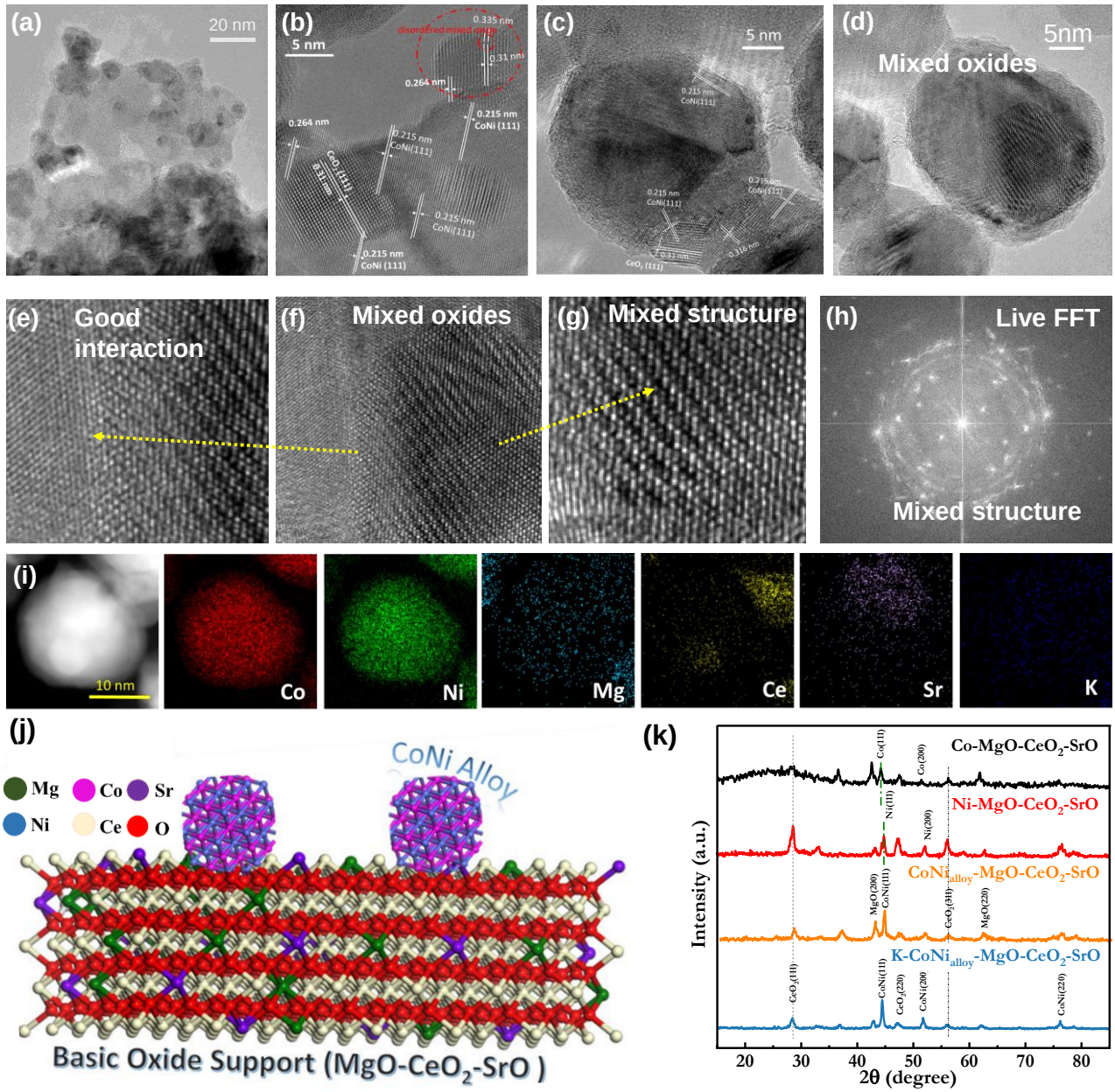

**Figure 1.** Morphological analysis of different catalysts. (a) TEM and (b-d) HRTEM, (e-g) HRTEM of overlapped lattice planes of the heterostructure, (h) FFT of respective mixed heterostructure, (i) HADF-STEM mapping of K-$CoNi_{alloy}$-MgO-$CeO_2$-SrO along with elemental mapping, (j) schematic illustration for the decorated $CoNi_{alloy}$ on the oxide support of MgO-$CeO_2$-SrO, and (k) XRD pattern of K-$CoNi_{alloy}$-MgO-$CeO_2$-SrO and comparative catalysts.

The high-resolution transmission electron microscopy (HR-TEM) images of the K-$CoNi_{alloy}$-MgO-$CeO_2$-SrO catalyst presented a uniform distribution of support nanoparticles (NPs) with CoNi alloy NPs (**Figure 1a**). These images clearly present defined crystalline structures for each compound phase. The prominent interlayer spacing of $CeO_2$ (0.31 nm) with (111) plane was found around the CoNi (111) interlayer spacing of 0.215 nm. MgO with a *d*-spacing of 0.264 nm was also identified using dotted circles (**Figure 1b-d, Figure S1**). The heterostructure of the K-$CoNi_{alloy}$-MgO-$CeO_2$-SrO catalyst is apparent among mixed oxide particles **(Figure 1d-g)**. The moire fringes indicate that crystal lattice planes with different spacing and/or orientation are overlapped, suggesting intimate interactions and possible chemical bonding among $CoNi_{alloy}$ and mixed oxides in heterostructure catalyst. Live Fast Fourier Transform (FFT) of the respective images also evidenced the mixed multimetal structure by disorder bright spots (**Figure 1h**). High-angle annular dark-field scanning TEM (HAADF-STEM) with EDS elemental mapping of the K-$CoNi_{alloy}$-MgO-$CeO_2$-SrO catalyst also displays a homogeneous distribution of Mg, Ce, Sr, and K in the mixed oxide support (**Figure 1i, Figure S2-4**). The multi-metal components may accommodate the local bonds during intercalation, resulting from strong interactions in the $CoNi_{alloy}$-MgO-$CeO_2$-SrO catalyst. The heterostructure interfaces likely lead to a synergistic effect to enhance the catalytic activity due to the

modification of geometric and electronic structures.[30] The mixed metal compositional interfaces could enhance the adsorption property of the reactants and dissociate into products at low activation energy.[31] The schematic illustration also presented the distribution of CoNi alloy nanoparticles with (111) phase on the mixed oxide support of MgO-$CeO_2$-SrO (**Figure 1j**). The crystal structures of the K-$CoNi_{alloy}$-MgO-$CeO_2$-SrO were studied using powder X-ray diffraction (XRD). The XRD patterns distinguish the CoNi alloy through prominent peaks at 44.32, 51.62, and 76.16° of CoNi and the distinct peaks associated with MgO and $CeO_2$ according to their standard JCPDS 75-1525, and 34-0394, respectively (**Figure 1k and Figure S5-6, SI**). The mean crystallite size of the CoNi alloy was calculated from Scherrer's equation using three peaks (*i.e.*, at 44.32, 51.62, and 76.16°). Higher content of Ce (Mg: Sr: Ce = 2:1:4) or Sr (Mg: Sr: Ce = 2:4:1) oxides caused larger CoNi crystallite sizes around 15.69 and 13.69 nm, respectively, likely causing relatively low $NH_3$ conversion efficiencies. The optimal Mg: Sr: Ce ratio of 2:1:1 in the oxide support corresponds to the smallest size of 8.7 nm of CoNi alloy, thereby generating increased active sites and promoting catalytic activity (**Table S1**). Therefore, the crystallite sizes of CoNi alloy are largely dependent on the composition of mixed oxide support, which is critical to catalytic activity.[32] The ratio among the elemental composition of mixed oxides was also further studied using XRD patterns. A prominent phase of MgO along with insignificant $CeO_2$ and SrO were identified in the optimal mixed oxide support (**Figure S7-8, Table S1, SI**). The K-$CoNi_{alloy}$-MgO-$CeO_2$-SrO catalyst presented the highest BET surface area of 30 $m^2/g$ than other supported catalysts (~20 $m^2/g$) (**Figure S9a** and **Table S2**). The pore size distribution curves indicate the maximum mesoporosity and microporosity in the best performing K-$CoNi_{alloy}$-MgO-$CeO_2$-SrO catalyst that facilitates the gas transport during the ADR. (**Figure S9b-g, Table S2, SI**).

### 2.2 Catalytic activity and stability for the ADR

Ammonia decomposition activity on the K-$CoNi_{alloy}$-MgO-$CeO_2$-SrO catalyst was studied in a fixed bed reactor with 4 mm ID and a 6 mm OD (**Figure S10**). The catalyst was activated under the flow of Ar gas at 600 $^oC$ for one hour before the testing. Then, the feed gas was immediately switched to pure $NH_3$ (>99.99%) at the target temperatures to determine $NH_3$ to $H_2$ conversion efficiencies. The gas hourly space velocity (GHSV) was calculated by using the catalytic mass loading (0.1 g) underflow of pure $NH_3$ gas flow (20 mL $min^{-1}$), which was determined to be 12000 mL $h^{-1}$ $g_{cat}^{-1}$.[17, 20, 26]. Meanwhile, we also used 0.3 g catalyst and the volume-based GHSV, *i.e.*, $h^{-1}$ to evaluate catalytic activity, which is more desirable for Ru-free nonprecious metal catalysts, as the amount of Ru-free catalysts is not a concern anymore. The $NH_3$ conversion efficiency was calculated by using **Equation S1**.

The K-$CoNi_{alloy}$-MgO-$CeO_2$-SrO catalyst achieved $NH_3$ conversion efficiencies of 97.7% and 87.50% at 450 $^oC$ at a GHSV of 6000 and 12000 mL $h^{-1}$ $g_{cat}^{-1}$, respectively (**Figure 2A**). The catalyst also presented a conversion efficiency of 93.50% at 450 $^oC$ and a volume-based GHSV of 6000 $h^{-1}$ (**Figure S11a**). The effect of K-promoter on the ammonia conversion efficiency was investigated by using different molarity of KOH during the catalyst preparation step (**Figure S12**). The optimized molarity (4.0 M KOH) in the initial synthesis steps generated the most significant K promotion effect in the catalyst. Generally, the K-promoter could donate electrons at the surface-active specie ($CoNi_{alloy}$) to promote the dinitrogen formation, which is a rate-determining step during the ADR process.[33] Comparatively, higher KOH molarity (5 M KOH) based catalyst exhibited lower conversion efficiency (86.2%) at 450 $^oC$ at a GHSV 6000 $h^{-1}$ because more K content can enhance the $K_2O$ rather than potassium metal and minimize the active sites for reaction process.[34]

To determine the role of each oxide in the catalytic activity of the K-$CoNi_{alloy}$-MgO-$CeO_2$-SrO catalyst, we investigated individual oxides (*i.e.*, MgO, $CeO_2$, and SrO), bimetallic oxide, and trimetallic oxides supported CoNi alloy catalyst for the ADR. The highest activity was obtained on the $CeO_2$ (68.7%), followed by the MgO (61.0%), and SrO (46.7%), which are all higher than the unsupported CoNi alloy catalyst (35%) at 450 °C. Furthermore, the activity can be substantially increased using the binary MgO-$CeO_2$ (73.89%) and the ternary MgO-$CeO_2$-SrO (87.7%) oxides at a GHSV of 12000 mL $h^{-1}$ $g_{cat}^{-1}$ (**Figure 2b and Figure S13**). Notably, only mixed oxide support (MgO-$CeO_2$-SrO) without CoNi alloy presented insignificant ADR activity with a conversion efficiency of 23% at a GHSV of 6000 mL $h^{-1}$ $g_{cat}^{-1}$ at 450°C (**Figure S14**). Various Co to Ni ratios (1:1, 2:1, 4:1, and 1:2) and mono metals (Co and Ni) in the same mixed oxide supported catalysts were studied concerning their ADR activities. The catalyst with a Co: Ni ratio of 2:1 generated the highest activity (**Figure S13**). Alloys often have distinct binding properties toward $NH_3$ and intermediates compared to their mono-metallic counterparts.[35] Also, the second metal may act as a pseudo ligand, either withdrawing or donating electrons, thereby modifying the electronic structure and creating a synergetic effect.[36] Furthermore, the effect of each component in the mixed oxide on catalyst performance by varying the molar ratios of Mg, Sr, and Ce was studied, and the highest activity was obtained from a ratio of Mg: Sr: Ce (2:1:1) in the range of 450 and 500 $^oC$ (**Figure S15-S16**). The addition of Sr into the mixed oxide of Mg and Ce is essential for improved catalytic activity, especially at the relatively low temperature (<500 $^oC$) and high GHSVs (> 20,000 $h^{-1}$) (**Figure S15**). Without Sr, ammonia conversion at 500 $^oC$ dropped to 64% at 20,000 $h^{-1}$. Several works also used Sr as a promoter or support for ADR catalysts and showed higher activity in the combination of multi-metals catalysts.[37, 38] In this work, the SrO has dual functions of promoter

and support in the heterostructured catalyst. The SrO has a good capability of electron-donating as a promoter and support, which modifies the electronic property of the catalyst. This electronic modification of the active sites by SrO species can facilitate recombinative nitrogen desorption in ADR reactions.[39] However, excessive Sr also leads to decreased activity (**Figure S16, SI**), either due to the formation of $Sr(OH)_2$ or an increase in CoNi crystallite size. Therefore, the optimal catalyst, consisting of CoNi alloy with 2:1 ratio on the ternary mixed oxide with 2:1:1 ratio of Mg, Ce, and Sr, exhibited the best activity at 450-500 $^{o}$C (**Figure 2c**). As for the promoter, when replaced K with Ce in the catalyst, the $NH_3$ conversion efficiency dropped from 100 to 89% at GHSV of 12000 mL $h^{-1}$ $g_{cat}^{-1}$ and 500 °C.

$H_2$ production rates were calculated using **Equation S2** and compared within a wide range of temperature and GHSV values. The K-$CoNi_{alloy}$-MgO-$CeO_2$-SrO catalyst can generate hydrogen at rates from 6.69 to 57.75 mmol $g_{cat}^{-1}$ $min^{-1}$ when GHSV values were increased from 6000 to 72000 mL $h^{-1}$ $g_{cat}^{-1}$ at 500 °C, respectively. (**Figure 2d** and **Figure S17**). The activity on the best performing K-$CoNi_{alloy}$-MgO-$CeO_2$-SrO catalyst was also calculated using different GHSV, *i.e.*, $h^{-1}$ and mL $g_{CoNi}^{-1}$ $h^{-1}$, which were further compared with reported Ru-free catalysts and Ru-based catalysts (**Table S3-4**). The K-$CoNi_{alloy}$-MgO-$CeO_2$-SrO catalyst reported in this work (53.56 $g_{NH3}$ $g_{metals}^{-1}$ $h^{-1}$) achieved much higher ADR activity compared to the state-of-the-art Ru-free catalyst in the literature[20], such as the HEA-$Co_{25}Mo_{45}$ (22.1 $g_{NH3}$ $g_{metals}^{-1}$ $h^{-1}$) at 500 $^{o}$C (**Figure 2e**).

The excellent stability of the best-performing K-$CoNi_{alloy}$-MgO-$CeO_2$-SrO catalyst was further determined in a fixed-bed reactor for 100 hours (**Figure S18a**). We also studied catalyst stability by changing temperatures dynamically from 400 $^{o}$C with around 50% conversion to 500 $^{o}$C with 100% conversion, showing outstanding stability (**Figure S18b**) and insignificant

changes in crystalline structures determined using XRD patterns ((**Figure S18c**). Furthermore, the catalyst was studied in a membrane reactor prototype designed by our industry team at Bettergy Corporation (Peekskill, NY) (**Figure S19)**. The remarkable stability of K-$CoNi_{alloy}$-MgO-$CeO_2$-SrO catalyst with complete $NH_3$ conversion was demonstrated in the membrane reactor at a GHSV of 12000 mL $h^{-1}$ $g_{cat}^{-1}$ and 500 $^oC$ for 600 hours under 1.5 bar (**Figure 2f**), only losing 1.0% degradation. According to XRD patterns before and after the long-term stability (**the inset of Figure 2f**), CoNi alloy and mixed oxides were well retained, showing no significant change in crystal structure/size. HR-TEM images for the catalyst after the stability test also indicated the well-retained CoNi alloy particles and apparent interfaces between metal and oxide supports (**Figure S20, SI**). Therefore, the exceptional catalyst stability is likely due to the mixed oxide surrounding the CoNi alloy NPs, which act as spacers and prevent sintering at high temperatures.

Notably, during the $NH_3$ decomposition, increasing pressures at the inlet can generate high-pressure $H_2$ at the outlet, which is desirable and reduces the subsequent compression cost. Hence, the effect of pressure on ammonia decomposition efficiency in a fixed bed reactor was first evaluated on the optimal catalyst. An increase in pressure from 1.0 to 5.0 bar led to a drop in $NH_3$ conversion (**Figure S21-22**), which can be explained using the Le Chatlier principle in a fixed bed reactor.[40] In contrast, a membrane reactor can shift the equilibrium forward direction by quickly removing produced $H_2$ even at higher pressures.[41] The above-mentioned prototype membrane (Pd composite zeolite) reactor has excellent $H_2$ separation from $N_2$ (**Figure S23**) but a limited capacity for $H_2$ generation (*e.g.*, 1-3 kg $H_2$/day). At 500 $^oC$, we achieved over 99% $NH_3$ conversion even at 5.0 bar and a reasonably high GHSV of 10,000 $h^{-1}$ with outstanding stability up to 120 hours (**Figure S23**). A detailed comparison of membrane reactors (**Table S5**)

and fixed-bed reactors (**Table S6**) reported recently for ammonia cracking is summarized with specific operation parameters. The combination of the Ru-free catalyst and the membrane reported in this work showed the best $NH_3$ cracking performance.

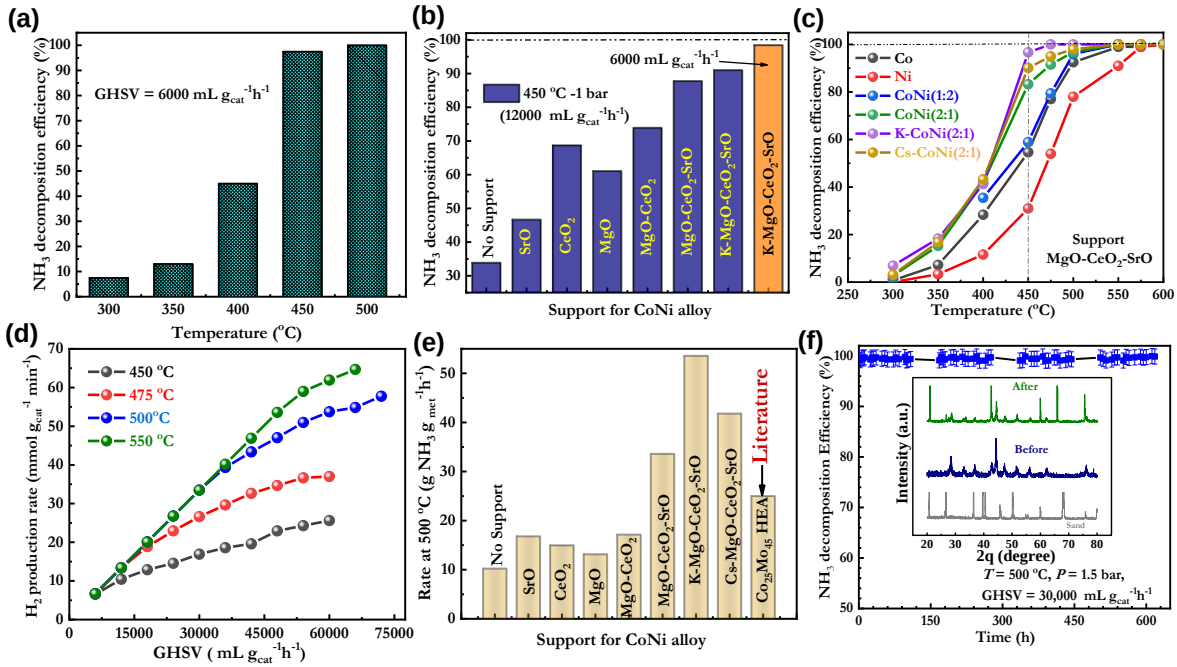


**Figure 2.** ADR activity and stability of K-CoNi$_{alloy}$-MgO-CeO$_2$-SrO catalyst. (a) ADR activity of K-CoNi$_{alloy}$-MgO-CeO$_2$-SrO at different reaction temperatures. (b) Comparison of $NH_3$ decomposition efficiency (with >99.99% $NH_3$) of K-CoNi$_{alloy}$-MgO-CeO$_2$-SrO with different mixed oxide support. (c) Comparison with different stoichiometry of CoNi, Ni, and Co on MgO-CeO$_2$-SrO at different temperatures. (d) Hydrogen production rate of K-CoNi$_{alloy}$-MgO-CeO$_2$-SrO catalyst at different temperatures. (e) $NH_3$ reaction rate for different developed ADR catalysts and literature catalysts. (f) Stability test at 500 °C with pure $NH_3$ over K-CoNi$_{alloy}$-MgO-CeO$_2$-SrO with a GHSV of mL $h^{-1}$ $g_{cat}^{-1}$ at 1.5 bar. The inset of f is the comparison of XRD before and after stability tests in a prototype membrane reactor.

### 2.3 Mechanistic understanding of active sites and activity improvements

To elucidate the active sites of the studied catalysts, we employed a micro-reactor to study $NH_3$ decomposition and monitored the mass spectroscopy (MS) signals of the outlet gases. The characterization allowed us to accurately determine the onset temperatures of the desorption of $N_2$ and $H_2$ during the $NH_3$ decomposition. The horizontal dash-dotted line shows zero ion current, whereas the vertical dotted line indicates the ion current at 450 °C for CoNi alloy particles on different types of support. The changes in the intensity of $NH_3$, $N_2$, and $H_2$ determined by using MS (**Figure 3a**) indicate a gradually enhanced activity from the studied mono, binary, and ternary mixed oxide supports with K promotion. The fastest decreasing rate of $NH_3$ intensity was observed with the best-performing K-$CoNi_{alloy}$-MgO-$CeO_2$-SrO catalyst. The variation of onset temperatures to generate $H_2$ and $N_2$ are compared in **Figures 3b** and **3c**, respectively. The onset temperature of $N_2$ desorption from the $CoNi_{alloy}$-MgO-$CeO_2$-SrO catalyst is around 275 $^oC$, around 120 $^oC$ lower than that from the unsupported CoNi alloy (~400 $^oC$). The desorption of both $H_2$ and $N_2$ was maximized at all temperatures for the CoNi alloy on the MgO-$CeO_2$-SrO support, followed by binary MgO-$CeO_2$, and then individual $CeO_2$, MgO, and SrO. Therefore, the micro-reactor combined with the more accurate MS analysis further verified the critical role of oxide supports and K promotion in boosting $NH_3$ decomposition. The multielement components may accommodate the local bonds during intercalation, resulting from strong interactions in multimetal phases. This heterostructure interface has presented a good synergistic effect to enhance the catalytic activity because of more active sites and tuned electronic properties. The apparent activation energies for the studied ADR catalysts were calculated from Arrhenius plots of $H_2$ production rates at different temperatures (**Figure 3d**). The best performing K-$CoNi_{alloy}$-MgO-$CeO_2$-SrO catalyst exhibited the lowest activation energy (56 kJ

$mol^{-1}$) as compared to less active catalysts and comparable to previously Ru-based reported catalysts.[20, 42] Among different explanations, the lowest activation energy could be due to the largest active sites at the surface of the catalyst for the ADR.[43, 44] **Figure 3e** compares the calculated turnover frequencies (TOFs) at 450, 475, and 500 $^{o}$C, respectively, for various catalysts. The number of active sites on various catalysts was determined by using the CO pulse chemisorption. At 450 $^{o}$C, the TOF of the $CoNi_{alloy}$-MgO-$CeO_2$-SrO catalyst is nearly two times higher than the CoNi alloy on MgO and 3-4 times higher than $CeO_2$ or SrO. With the $K^+$ promotion, the TOF values were further increased (**Table S6**), further validating the effectiveness of $K^+$ promoters for Co, Ni, and CoNi alloys at different temperatures (**Figure 3f**).

K-promoter could further regulate basicity of the catalyst. During ADR, the conversion rate increased as the electronegativity of the promoter reduced because alkaline metals cation produced atomic level interaction with the substrate.[45] The electron-donating promoters on the active species ($CoNi_{alloy}$) enhance the number of active sites for the N-adsorption/recombination and then desorption to $N_2$-gas.[37] Generally, catalyst support presents high basicity, conductivity, thermal stability, and surface area.[24] Basicity has also been related to active metals because ammonia dehydrogenation and recombination of adsorptive nitrogen atoms are the more likely rate-limiting steps of ADR. However, the basicity of the catalyst is modulated by the insertion of a promoter that enhances the electron-donating properties of the catalyst since promoters have an indirect role in inducing stronger basicity of high-performing catalysts. The relationship between electron-donating promoter and active metal depends on the direct electronic interaction with active metal. In short, the combination of basicity, the high electron-donating capacity of support, active materials, and promoters are major components of the best-performing catalyst.

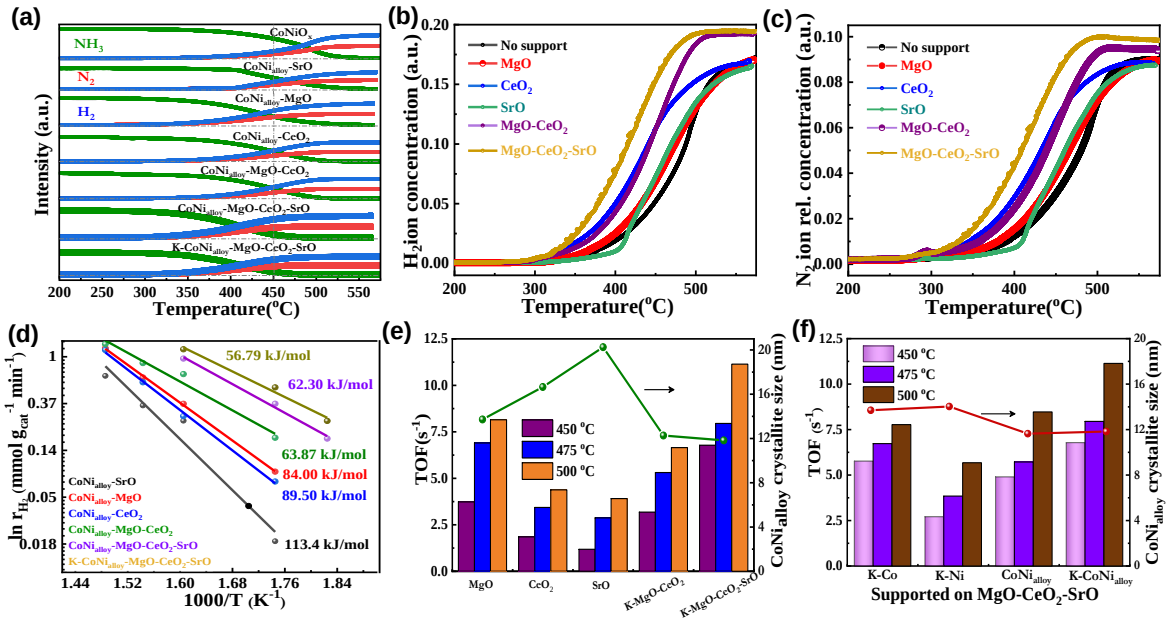


**Figure 3.** The influence of different conditions on catalytic performance. MS signals of (a) the outlet gases $NH_3$, $N_2$, and $H_2$ (green, red, and blue curves, respectively) over CoNi alloy on different types of support. (b) $H_2$ and (c) $N_2$ concentration at different temperatures over CoNi alloy on various supports. (d) The activation energy of different metal NPs on the mixed oxide MgO- $CeO_2$-SrO. (e-f) TOF and crystallite size comparison of (e) CoNi alloy on different supports and (f) different metal NPs on the optimal MgO-$CeO_2$-SrO support.

Furthermore, the reduction temperatures of oxides and CoNi alloys were determined using $H_2$ temperature-programmed reduction ($H_2$-TPR) (**Figure 4a-b**). The temperature was increased from 25 to 600 °C to study the effect of various oxide supports on the oxidation state of CoNi alloy as well as the reducibility of Co and Ni species during the ammonia decomposition process. Upon deconvolution, four major peaks are observed (**Figure 4a**). The 1st peak can be associated with the reduction of $Co_3O_4$ to CoO, followed by reductions of CoO to Co (2nd peak) and NiO to Ni (3rd peak).[46] The fourth peak at above 600 °C is probably due to the reduction of the mixed

oxides. Due to the strong interaction with oxide supports, cobalt oxides require a higher temperature to be reduced. The reduction temperatures of CoNi on the MgO-$CeO_2$-SrO support are the lowest, followed by the individual SrO, $CeO_2$, and MgO supports. In principle, the changes in particle sizes could shift reduction temperatures.[47] Therefore, the relatively low reducing temperature is likely due to the smallest sizes of the CoNi alloy on the mixed oxide support (**Table S7**). In addition to the size effect, the reducing temperatures are dependent on the nature of oxides and their interactions with deposited metal particles. For example, a reduction peak of pure $CeO_2$ at 800 $^oC$ is higher than a mixed oxide (*i.e.*, $CeO_2$-$TiO_2$) at ~550 $^oC$ and the same oxide with Ni deposition at 350 $^oC$.[48] Similarly, the reduction peak shifts to lower temperatures for the mixed oxide, compared to individual $CeO_2$. Likewise, the reduction temperature for the CoNi-$CeO_2$ is lower than $CeO_2$ alone. We further compared the $H_2$-TPR profiles for the unsupported CoNi, CoNi-MgO-$CeO_2$-SrO, and K-CoNi-MgO-$CeO_2$-SrO. Although the crystallite size of the K-CoNi-MgO-$CeO_2$-SrO is the smallest, its reduction temperature range is overall higher than the CoNi-MgO-$CeO_2$-SrO. There is no reduction peak at temperatures above 600 $^oC$ for the unsupported CoNi alloy particles. The reduction peaks at 700 $^oC$ for the CoNi-MgO-$CeO_2$-SrO and K-CoNi-MgO-$CeO_2$-SrO catalysts are probably due to the partial reduction of ternary mixed oxide. Thus, the $H_2$-TPR study confirmed a complete reduction of the CoNi alloy at 600 $^oC$. The finding guides us to activate the CoNi catalysts at 600 $^oC$ under forming gas for the best activity before performing the $NH_3$ decomposition.

During the $H_2$-TPR, $H_2$ consumption could be an indicator of the CoNi oxides content, which can determine the interaction between the CoNi alloy and various supports. Compared to the CoNi-MgO (260.44 mL/g) and CoNi-$CeO_2$ (315.23 mL/g), the $H_2$ consumption of the CoNi-MgO-$CeO_2$-SrO (219.22 mL/g) catalyst is smaller. The decreased $H_2$ consumption could be

related to the stronger interaction of CoNi alloys with the mixed metal oxide support compared to the single metal oxide supports. Also, low $H_2$ consumption for the mixed oxide support could be due to enhanced thermal stability of the mixed oxide support relative to individual ones during the $NH_3$ decomposition.

Basicity is a critical factor for the high-performance ADR catalyst. $CO_2$-temperature-programmed desorption (TPD) was carried out to determine the basicity of the K-$CoNi_{alloy}$-MgO-$CeO_2$-SrO catalyst (**Figure 4c-d**). The desorption, which appears in the range of 100 to 425 $^oC$, indicates $CO_2$ desorption from weak basic sites. In contrast, peaks beyond 550 $^oC$ correspond to the presence of strong basic sites.[49] Desorption peaks between the two temperatures correspond to medium basic sites. The weak sites are related to lattice-bound and isolated hydroxyl groups exhibiting Brønsted basicity.[49] In contrast, the medium and strong basic sites are ascribed to three- and/or four-fold-coordinated $O^{2-}$ anions, *i.e.*, Lewis basicity.[49] In principle, medium and strong basic sites are critical to $NH_3$ decomposition through improving the $N_2$ desorption due to facilitated electron transfer.[50] Regarding the metal particles, the basicity order is Ni < Co < $CoNi_{alloy}$ < K-$CoNi_{alloy}$, which is in good agreement with their catalytic activity (**Figure 4c**). Among the oxides, the K-promoted MgO-$CeO_2$-SrO support exhibits the strongest basic sites, followed by the MgO-$CeO_2$-SrO, MgO-$CeO_2$, MgO, $CeO_2$, and SrO (**Figure 4d** and **Table S7**). Moreover, the TOFs for the K-$CoNi_{alloy}$-MgO-$CeO_2$-SrO, and developed catalysts of $CoNi_{alloy}$ on different supports were calculated by using the $H_2$ production rate and active site density determined by CO pulse chemisorption (**Equation S3**). The K-$CoNi_{alloy}$-MgO-$CeO_2$-SrO catalyst exhibited the higher TOFs values of 6.78, 7.94, and 11.14 $s^{-1}$ at temperature of 450, 475 and 500˚C, respectively (**Table S8**).

High-resolution *ex-situ* XPS of the as-prepared K-$CoNi_{alloy}$-MgO-$CeO_2$-SrO was analyzed to determine the chemical bonding among CoNi alloy and mixed metal oxide support. The deconvoluted Co 2p and Ni 2p XPS spectra of active species CoNi alloy exhibited metallic states of Co and Ni along with significant oxide species such as $Co^{2+}$ (779.4 eV) and $Ni^{2+}$ (855.2 eV) likely oxidized under air atmosphere (**Figure S24**).[51] The deconvoluted XPS spectra of Mg 2p, Ce 3d, and Sr 3d also confirmed the oxidation states of the MgO-$CeO_2$-SrO support (**Figure S24c-e**). Furthermore, we performed *in-situ* high-temperature XPS spectra after exposing the catalyst to temperatures between 100 and 600 $^oC$ in pure $H_2$, similar to the actual ADR at high temperatures (**Figure S25-S26**). At 100 $^oC$, both Co and Ni were found in their +2 and +3 state, respectively, similar to ex-situ XPS results. Zero valent states of Co and Ni are apparent when reduced at 200 $^oC$ along with their oxidation states. No peak was observed corresponding to +3 valence state at 400 and 500 $^oC$. At 600 $^oC$, all Co and Ni oxidation states disappear in the best performing K-$CoNi_{alloy}$-MgO-$CeO_2$-SrO catalyst. The *in-situ* observation confirmed that the complete metallic CoNi alloy, instead of their oxides, is likely the active site.

The *in-situ* XPS experiments for the optimal catalyst under $NH_3$ atmosphere at various operating temperatures from 400 to 600 $^oC$ were carried out. **Figure 4e-i** show the XPS spectra for Co 2p, Ni 2p, Ce 3d, Mg 1s, and Sr 3d, respectively, after *in-situ* heating at the relevant 500 $^oC$ under an $NH_3$ atmosphere. No oxide peak is observed for Co and Ni. A small peak is observed for their corresponding nitrides. The N content in the catalyst developed at each temperature is low. The maximum N content of about 2 wt.% was observed at 600 $^oC$. Thus, in the presence of $NH_3$, the alloy does not significantly convert into corresponding nitrides. The observation is similar to those at 400 and 600 $^oC$. Again, metallic CoNi species rather than their nitrides are the actual active sites for the ADR. Ceria presented in a mixed-valence state of $Ce^{4+}/Ce^{3+}$ as

observed from the *in-situ* XPS at 500 °C (**Figure 4g**). Ce has a unique $Ce^{4+}/Ce^{3+}$ redox associated with the formation of oxygen vacancies at the surface,[52,53] which may be critical for the $NH_3$ decomposition. Most of the $Mg^{2+}$ and $Sr^{2+}$ species are still in the oxide form under $NH_3$ at 500 °C (**Figure 4h-i, Figure S27-28**). Combining the XRD pattern and the *in-situ* XPS analysis, the dominant MgO and $CeO_2$ provide a primary matrix with Sr doping, further increasing the basicity of the ternary support for improved ammonia decomposition efficiency.

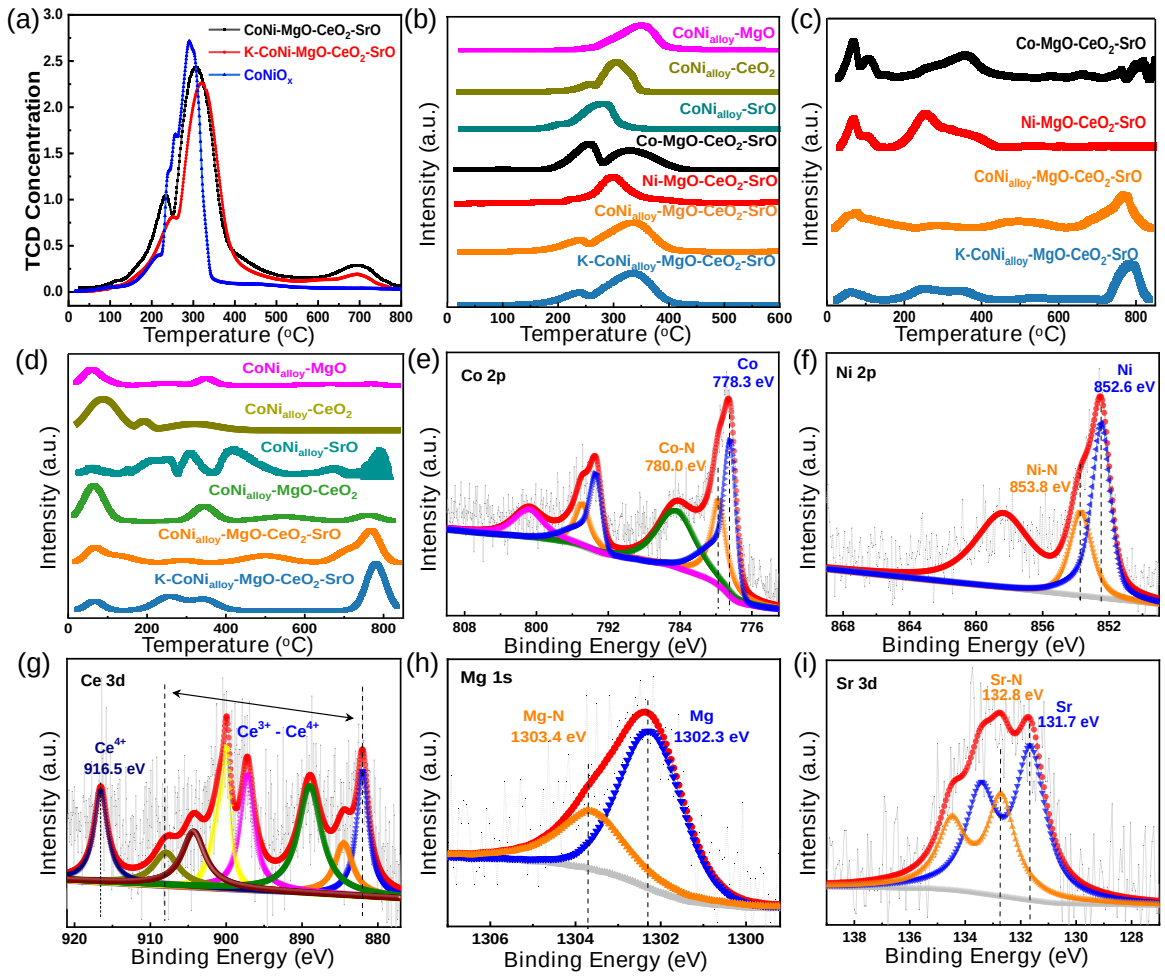


**Figure 4.** Comparison of different catalyst structures. (a-b) Deconvoluted $H_2$-TPR profiles for CoNi alloy catalysts on different supports. (c, d) $CO_2$-TPD for studied catalysts. (e-i) In situ XPS

analysis of the K-$CoNi_{alloy}$-MgO-$CeO_2$-SrO under $NH_3$ at 500 $^oC$ of (e) Co 2p, (f) Ni 2p, (g) Ce 3d, (h) Mg 1s, and (i) Sr 3d.

### 2.4 DFT Calculations

To unveil the possible synergy in the heterostructure catalyst, we further performed DFT calculations to predict the critical role of CoNi alloy, metal oxides, and their interactions in promoting ADR (**Figure 5**). The simplified energy profiles of ammonia dissociation on different models are presented for Co (111), $Co_2Ni$ (111), $CoNi_2$ (111), Ni (111), and $CeO_2/Co_2Ni$ (111) (**Figure 5a**). The details of adsorption sites, adsorption energies, and activation energy for each elementary step have also been provided in detail (**Figure S29-S30** and **Table S9-S10**). As shown in the reaction energy profiles, the rate-limiting step for ammonia dissociation on the metal surfaces, including the alloy surfaces, is the re-combinative desorption of N adatoms, following the N-H bond cleavage.

To understand the difference in reactivity between pure metals, the alloys, and the influence of the supported oxide, we performed Bader charge analysis and provided the Bader charges of the metal atoms in the top layer of the slab (**Figure 5b** and **Figure S31**). The surface atoms of pure Co and Ni are negatively charged. In contrast, at the CoNi alloy surface, the Co atoms are positively charged, whereas the Ni atoms have negative partial charges, creating a localized charge polarization. These locally polarized sites are considered more active for ammonia adsorption and dissociation on the alloy surfaces. Thus, the bimetallic CoNi catalysts are predicted to be more active than the pure Co or Ni for ammonia dissociation, which agrees with the experimental results presented in this work.

Importantly, the dramatically enhanced catalytic activity of the CoNi alloy reported in this work is primarily due to the unique interfaces between the CoNi alloy and the ternary oxide support. This is illustrated by the potential energy profile of $N_2$ formation from N adatoms on the alloy surface with (right-hand) and without (left-hand) oxide interfaces (**Figure 5c**). As shown in **Figure S32**, N adatoms form on the alloy surface following the complete N-H bonds cleavage, which is consistent with the *in-situ* XPS results, evidenced by the sole presence of N on the alloy surface. The N adatoms diffuse at the catalyst surface and recombine to form $N_2$. This step needs to overcome a significantly high activation barrier on the alloy surface, *i.e.*, 1.52 eV over $Co_2Ni$. Alternatively, the N atoms can diffuse toward the oxide/metal interfaces and then recombine and desorb as $N_2$. The activation barrier for the re-combinative desorption at the metal/oxide interfaces, such as $CeO_2/Co_2Ni$ (0.82 eV) and $MgO/Co_2Ni$ (0.89 eV), is significantly decreased relative to the alloy surface. Thus, the metal/oxide interfaces play an important role in accelerating the recombination of N adatoms and enhancing activity.

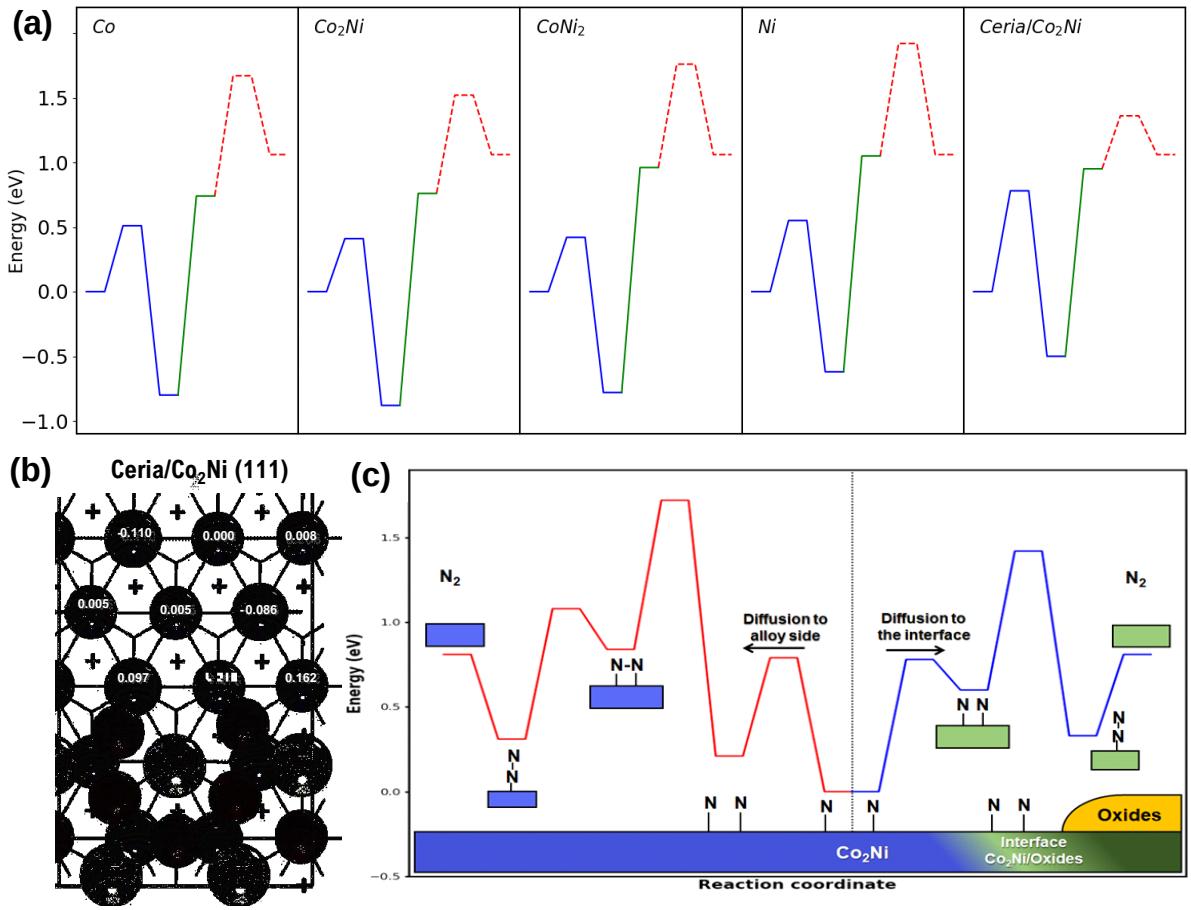


**Figure 5.** Theoretical analysis of the critical role of CoNi alloy, metal oxides, and their interactions in promoting ammonia decomposition. (a) Simplified energy profiles of $NH_3$ decomposition and $N_2$ formation on Co (111), $Co_2Ni$ (111), $CoNi_2$ (111), Ni (111), and $CeO_2/Co_2Ni$ (111). C-H bond cleavage, $H_2$ desorption, and N-N re-combinative desorption are represented by blue lines, green lines, and red dashed lines, respectively. (b) Top view of the surface unit cells of the $CeO_2/Co_2Ni$ (111). Also shown are the Badger charge values of the surface metal atoms. (c) The energy profiles of $NH_3$ dissociation and $N_2$ formation on alloy (left side) and alloy-oxide interfaces (right side). Studied oxides include $CeO_2$ and MgO, showing the same trends.

As shown by the potential energy profiles in **Figure 5c**, the activation barriers for N adatom diffusion to the interfacial site and on the alloy surface are similar (~0.39 eV), supporting that the interfacial sites are likely the favorable activate sites for $N_2$ desorption. Consequently, the highest experimentally observed activity of the ternary oxide-supported CoNi alloy catalyst can be attributed to the smallest crystallite size, which creates an increased number of active sites at the metal/oxide interfaces for $N_2$ desorption.

## 3. Conclusion

In summary, we developed a high-performance and sustainable Ru-free catalyst for $NH_3$ decomposition, which is crucial for on-site hydrogen generation to address hydrogen storage and transportation issues. The present work reports an effective strategy for designing a heterostructure catalyst through identifying the appropriate active metal species, mixed oxide support, and promoters for the ADR. The catalyst consists of CoNi alloy nanoparticles (Co: Ni = 2:1) on K-modified ternary mixed oxide MgO-$CeO_2$-SrO support with appropriate ratios. As a result, the best performing K-$CoNi_{alloy}$-MgO-$CeO_2$-SrO catalyst exhibited 97.7% and 87.50% $NH_3$ conversion efficiency at 450 $^oC$ at GHSVs of 6000 and 12000 mL $h^{-1}$ $g_{cat}^{-1}$, respectively. At 500 $^oC$, the catalyst can achieve an encouraging $H_2$ production rate (57.75 mmol $g_{cat}^{-1}$ $min^{-1}$), comparable to most of the reported Ru-based catalysts. Moreover, the compelling catalyst performance was further demonstrated in a membrane reactor prototype, showing excellent stability up to 600 hours at 500 $^oC$ and 1.5 bar without apparent degradation. The unique $Ce^{3+}/Ce^{4+}$ redox from $CeO_x$ in the mixed oxide support facilitates the uniform dispersion of the CoNi alloy nanoparticles with the smallest crystallite size. The increased basicity is crucial for the enhanced catalytic performance, which can be further increased by the Sr addition into MgO and $CeO_2$ and the additional K promoters. The ratio of Co and Ni in alloys is critical to

maximizing the catalytic performance. Each component of the ternary metal oxides has been carefully investigated concerning their interactions with dispersed CoNi alloy nanoparticles, optimal basicity, and stability. The $MgO_x$ serves as the primary framework for ternary metal oxide support due to its well-known basic properties.

DFT calculations confirmed the optimal Co: Ni ratio in the alloy catalyst to achieve enhanced performance as compared to the single metal and other alloy catalysts. More importantly, the active sites at the metal/oxide interfaces facilitate the recombination of the adsorbed N atoms and the subsequent $N_2$ desorption with a significantly reduced activation energy barrier. We believe that the remarkable activity and stability were due to high surface area, mixed oxides support, small crystallite size, electron-donating promoters, multi-metal active interface, strong interactions among multiphase active species, and favorable activate sites for $N_2$ desorption. Therefore, this is the first Ru-free catalyst that exhibited outstanding performance, approaching complete $NH_3$ conversion at economically feasible 450 $^oC$ for clean on-site hydrogen generation. This work would stimulate more research on developing advanced ammonia cracking technologies using earth-abundant materials, which is the key to the sustainable hydrogen economy.

Further engineering the catalyst nanostructures and morphologies (*e.g.*, porosities, sizes, and surface areas) is crucial for achieving complete $NH_3$ conversion at higher GHSVs and higher pressures (up to 40 bar) for practical application in the future. Scaling up the catalyst synthesis from grams to industrially relevant quantities while maintaining the ideal dispersion and other characteristics remains a grand challenge. Low-Co or Co-free catalysts are desirable due to the relatively high cost of Co and a major human rights issue associated with its production at present.

## Author Contributions

G.W., S.M., and H.T conceived the concept and designed all experimental studies. S.M., H.T., and X.Y. synthesized the catalysts and carried out conventional material characterization under the supervision of G.W.. The DFT calculations were performed by D.H. and T.Z under the supervision of Q.F.. S.K. carried out *ex-situ* and *in-situ* XPS analysis. S.H. performed electron microscopy analysis. J.C. and E.A.K. carried out TPR, TPD, and micro-reactor studies. M.C., B.L., and Z.T. scaled up catalysts and conducted the long-term stability tests in a prototype membrane reactor. H.T. and G.W. wrote the paper in consultation with all authors.

## Conflicts of interest

The authors have filed a US provisional patent application (No. 16/920,056) through the University at Buffalo and Bettergy Corp. on the catalysts described herein. The inventors are G. Wu, S. Mukherjee, Z. Tang, and B. Lu. The remaining authors declare no competing interests.

## Acknowledgments

This work was financially supported by the U.S. Department of Energy's Advanced Research Projects Agency-Energy (ARPA-E) Office's REFUEL program (Award No. DE-AR0000817), and partially supported by the New York State Energy Research and Development Authority (NYSERDA) under Agreement No. 141102. Electron microscopy research was conducted at the Brookhaven National Laboratory, the DOE Office of Science User Facilities. Q.G. acknowledges the support of the National Science Foundation (NSF-CBET, No.1438440).

## References

1. R. F. SERVICE, *Science*, 2018, doi: 10.1126/science.aau7489.
2. D. E. H. J. Gernaat, H. S. de Boer, V. Daioglou, S. G. Yalew, C. Müller and D. P. van Vuuren, *Nature Climate Change*, 2021, **11**, 119-125.
3. J. E. Givens, S. O. Hazboun, M. D. Briscoe and R. S. Krannich, *Society & Natural Resources*, 2021, **34**, 99-121.
4. R. W. Howarth and M. Z. Jacobson, *Energy Science & Engineering*, 2021, **9**, 1676-1687.
5. I. Staffell, D. Scamman, A. Velazquez Abad, P. Balcombe, P. E. Dodds, P. Ekins, N. Shah and K. R. Ward, *Energy & Environmental Science*, 2019, **12**, 463-491.
6. H. Tabassum, W. Guo, W. Meng, A. Mahmood, R. Zhao, Q. Wang and R. Zou, *Advanced Energy Materials*, 2017, **7**, 1601671.
7. U. Eberle, M. Felderhoff and F. Schüth, *Angewandte Chemie International Edition*, 2009, **48**, 6608-6630.
8. M. Li, Z. Zhao, T. Cheng, A. Fortunelli, C.-Y. Chen, R. Yu, Q. Zhang, L. Gu, B. V. Merinov and Z. Lin, *Science*, 2016, **354**, 1414-1419.
9. G. Wu, K. L. More, C. M. Johnston and P. Zelenay, *Science*, 2011, **332**, 443-447.
10. L. Schlapbach and A. Züttel, in *Materials for Sustainable Energy*, Co-Published with Macmillan Publishers Ltd, UK, 2010, DOI: doi:10.1142/9789814317665_0038

10.1142/9789814317665_0038, pp. 265-270.

11. P. Nikolaidis and A. Poullikkas, *Renewable and Sustainable Energy Reviews*, 2017, **67**, 597-611.
12. M. Aziz, A. T. Wijayanta and A. B. D. Nandiyanto, *Energies*, 2020, **13**, 3062.
13. S. Mukherjee, S. V. Devaguptapu, A. Sviripa, C. R. F. Lund and G. Wu, *Applied Catalysis B: Environmental*, 2018, **226**, 162-181.

14. M. Młotek, M. Perron and K. Krawczyk, *Energy Technology*, 2021, **9**, 2100677.
15. S. Chatterjee, R. K. Parsapur and K.-W. Huang, *ACS Energy Letters*, 2021, **6**, 4390-4394.
16. J. Guo and P. Chen, *Accounts of Chemical Research*, 2021, **54**, 2434-2444.
17. C. Chen, K. Wu, H. Ren, C. Zhou, Y. Luo, L. Lin, C. Au and L. Jiang, *Energy & Fuels*, 2021, **35**, 11693-11706.
18. C. Huang, Y. Yu, J. Yang, Y. Yan, D. Wang, F. Hu, X. Wang, R. Zhang and G. Feng, *Applied Surface Science*, 2019, **476**, 928-936.
19. I. Lucentini, G. García Colli, C. D. Luzi, I. Serrano, O. M. Martínez and J. Llorca, *Applied Catalysis B: Environmental*, 2021, **286**, 119896.
20. P. Xie, Y. Yao, Z. Huang, Z. Liu, J. Zhang, T. Li, G. Wang, R. Shahbazian-Yassar, L. Hu and C. Wang, *Nature Communications*, 2019, **10**, 4011.
21. I. Lucentini, X. Garcia, X. Vendrell and J. Llorca, *Industrial & Engineering Chemistry Research*, 2021, DOI: 10.1021/acs.iecr.1c00843.
22. J. W. Makepeace, T. J. Wood, H. M. A. Hunter, M. O. Jones and W. I. F. David, *Chemical Science*, 2015, **6**, 3805-3815.
23. K. F. Ortega, D. Rein, C. Lüttmann, J. Heese, F. Özcan, M. Heidelmann, J. Folke, K. Kähler, R. Schlögl and M. Behrens, *ChemCatChem*, 2017, **9**, 659-671.
24. T. E. Bell and L. Torrente-Murciano, *Topics in Catalysis*, 2016, **59**, 1438-1457.
25. J. Cha, T. Lee, Y.-J. Lee, H. Jeong, Y. S. Jo, Y. Kim, S. W. Nam, J. Han, K. B. Lee, C. W. Yoon and H. Sohn, *Applied Catalysis B: Environmental*, 2021, **283**, 119627.
26. K. Ogasawara, T. Nakao, K. Kishida, T.-N. Ye, Y. Lu, H. Abe, Y. Niwa, M. Sasase, M. Kitano and H. Hosono, *ACS Catalysis*, 2021, **11**, 11005-11015.

27. T. E. Bell, H. Ménard, J. M. González Carballo, R. Tooze and L. Torrente-Murciano, *International Journal of Hydrogen Energy*, 2020, **45**, 27210-27220.
28. S. Podila, H. Driss, S. F. Zaman, A. M. Ali, A. A. Al-Zahrani, M. A. Daous and L. A. Petrov, *International Journal of Hydrogen Energy*, 2020, **45**, 873-890.
29. D. V. Leybo, A. N. Baiguzhina, D. S. Muratov, D. I. Arkhipov, E. A. Kolesnikov, V. V. Levina, N. I. Kosova and D. V. Kuznetsov, *International Journal of Hydrogen Energy*, 2016, **41**, 3854-3860.
30. P.-C. Chen, M. Liu, J. S. Du, B. Meckes, S. Wang, H. Lin, V. P. Dravid, C. Wolverton and C. A. Mirkin, *Science*, 2019, **363**, 959-964.
31. X. Chen, X. Wang, X. Zhang, D. Liu, K. Srinivas, F. Ma, B. Wang, B. Yu, Q. Wu and Y. Chen, *International Journal of Hydrogen Energy*, 2021, **46**, 35198-35208.
32. Y. Zhu, J. Sokolowski, X. Song, Y. He, Y. Mei and G. Wu, *Advanced Energy Materials*, 2020, **10**, 1902844.
33. B. Lin, K. Wei, X. Ma, J. Lin and J. Ni, *Catalysis Science & Technology*, 2013, **3**, 1367-1374.
34. Z. Tian, C. Wang, J. Yue, X. Zhang and L. Ma, *Catalysis Science & Technology*, 2019, **9**, 2728-2741.
35. R. Ferrando, J. Jellinek and R. L. Johnston, *Chemical Reviews*, 2008, **108**, 845-910.
36. M. H. Rashid, M. Raula and T. K. Mandal, *Journal of Materials Chemistry*, 2011, **21**, 4904-4917.
37. I. Lucentini, X. Garcia, X. Vendrell and J. Llorca, *Industrial & Engineering Chemistry Research*, 2021, **60**, 18560-18611.

38. K. Sakaki, T. Yamada, M. Mizuno, H. Araki and Y. Shirai, *MATERIALS TRANSACTIONS*, 2002, **43**, 2652-2655.
39. M. Chen, M. Yuan, J. Li and Z. You, *Applied Catalysis A: General*, 2018, **554**, 1-9.
40. D. G. Löffler and L. D. Schmidt, *Journal of Catalysis*, 1976, **41**, 440-454.
41. S. H. Israni, B. K. R. Nair and M. P. Harold, *Catalysis Today*, 2009, **139**, 299-311.
42. X. Ju, L. Liu, P. Yu, J. Guo, X. Zhang, T. He, G. Wu and P. Chen, *Applied Catalysis B: Environmental*, 2017, **211**, 167-175.
43. A. M. Karim, V. Prasad, G. Mpourmpakis, W. W. Lonergan, A. I. Frenkel, J. G. Chen and D. G. Vlachos, *Journal of the American Chemical Society*, 2009, **131**, 12230-12239.
44. S. F. Yin, B. Q. Xu, W. X. Zhu, C. F. Ng, X. P. Zhou and C. T. Au, *Catalysis Today*, 2004, **93-95**, 27-38.
45. D. Cheddie, *Hydrogen Energy - Challenges and Perspectives*, 2012, 333−362.
46. O. A. Bulavchenko, E. Y. Gerasimov and T. N. Afonasenko, *Dalton Transactions*, 2018, **47**, 17153-17159.
47. C. e. Li, L. Wong, L. Tang, N. V. Y. Scarlett, K. Chiang, J. Patel, N. Burke and V. Sage, *Applied Catalysis A: General*, 2017, **537**, 1-11.
48. C. Ruan, Z.-Q. Huang, J. Lin, L. Li, X. Liu, M. Tian, C. Huang, C.-R. Chang, J. Li and X. Wang, *Energy & Environmental Science*, 2019, **12**, 767-779.
49. X. Guo, Y. Li, R. Shi, Q. Liu, E. Zhan and W. Shen, *Applied Catalysis A: General*, 2009, **371**, 108-113.
50. M. Miyamoto, A. Hamajima, Y. Oumi and S. Uemiya, *International Journal of Hydrogen Energy*, 2018, **43**, 730-738.

51. L. Chen, Z. Xu, W. Han, Q. Zhang, Z. Bai, Z. Chen, G. Li and X. Wang, *ACS Applied Nano Materials*, 2020, **3**, 1354-1362.
52. X. Zhao, X. Yang, M. Wang, S. Hwang, S. Karakalos, M. Chen, Z. Qiao, L. Wang, B. Liu, Q. Ma, D. A. Cullen, D. Su, H. Yang, H.-Y. Zang, Z. Feng and G. Wu, *Applied Catalysis B: Environmental*, 2020, **279**.
53. S. Toemen, W. A. W. Abu Bakar and R. Ali, *Journal of CO2 Utilization*, 2016, **13**, 38-49.